Contents lists available at ScienceDirect

Osteoarthritis and Cartilage Open

Imaging mass cytometry reveals tissue-specific cellular immune phenotypes in the mouse knee following ACL injury

Sanique M. South [a,b,h], M. Caleb Marlin [c,h], Padmaja Mehta-D'souza [a], Tayte Stephens [c], Taylor Conner [a], Kevin G. Burt [d,e], Joel M. Guthridge [c], Carla R. Scanzello [d,e], Timothy M. Griffin [a,f,g,*]

[a] Aging and Metabolism Research Program, Oklahoma Medical Research Foundation, Oklahoma City, OK, 73104, USA
[b] Phil and Penny Knight Campus for Accelerating Scientific Impact, University of Oregon, Eugene, OR, 97403, USA
[c] Arthritis and Clinical Immunology Research Program, Oklahoma Medical Research Foundation, Oklahoma City, OK, 73104, USA
[d] Translational Musculoskeletal Research Center & Department of Medicine, Corporal Michael J. Crescenz Department of Veterans Affairs Medical Center, Philadelphia, PA, 19104, USA
[e] Division of Rheumatology, University of Pennsylvania Perelman School of Medicine, Philadelphia, PA, 19104, USA
[f] Oklahoma City VA Health Care System, Oklahoma City, OK, 73104, USA
[g] Oklahoma Center for Geroscience and the Department of Biochemistry and Molecular Biology, University of Oklahoma Health Sciences Center, Oklahoma City, OK, 73104, USA

ARTICLE INFO

ABSTRACT

Objective: To develop an imaging mass cytometry method for identifying complex cell phenotypes, inter-cellular interactions, and population changes in the synovium and infrapatellar fat pad (IFP) of the mouse knee following a non-invasive compression injury.

Design: Fifteen male C57BL/6 mice were fed a high-fat diet for 8 weeks prior to random assignment to sham, 0.88 mm, or 1.7 mm knee compression displacement at 24 weeks of age. 2-weeks after loading, limbs were prepared for histologic and imaging mass cytometry analysis, focusing on myeloid immune cell populations in the synovium and IFP.

Results: 1.7 mm compression caused anterior cruciate ligament (ACL) rupture, development of post-traumatic osteoarthritis, and a 2- to 3-fold increase in cellularity of synovium and IFP tissues compared to sham or 0.88 mm compression. Imaging mass cytometry identified 11 myeloid cell subpopulations in synovium and 7 in IFP, of which approximately half were elevated 2 weeks after ACL injury in association with the vasculature. Notably, two monocyte/macrophage subpopulations and an MHC II^{hi} population were elevated 2-weeks post-injury in the synovium but not IFP. Vascular and immune cell interactions were particularly diverse in the synovium, incorporating 8 unique combinations of 5 myeloid cell populations, including a monocyte/macrophage population, an MHC II^{hi} population, and 3 different undefined F4/80$^+$ myeloid populations.

Conclusions: Developing an imaging mass cytometry method for the mouse enabled us to identify a diverse array of synovial and IFP vascular-associated myeloid cell subpopulations. These subpopulations were differentially elevated in synovial and IFP tissues 2-weeks post injury, providing new details on tissue-specific immune regulation.

1. Introduction

Osteoarthritis (OA) is a debilitating joint disease involving changes in joint tissue structure, peripheral pain sensitization, and impaired function. A central factor of these pathologic features is inflammation due to innate immune activity [1], although the precise mechanisms remain elusive. Mild systemic inflammation measured by high sensitivity serum C-reactive protein is associated with elevated risk for painful OA

[2]. In addition, an exploratory secondary analysis of a large, multi-year randomized trial involving IL-1β inhibition with canakinumab reported a reduction in the rate of incident total hip or knee replacement of individuals with active treatment versus placebo [3]. Yet shorter duration anti-inflammatory clinical trials have failed to meet outcomes. A barrier to the development of new targeted therapies is an incomplete understanding of the diverse cellular and molecular inflammatory mediators of OA pathology and symptoms. Recent studies highlight potential differences due to disease endotype, disease stage, gender, and joint specificity [4,5]. Here we focused on identifying tissue-specific cellular inflammatory mediators following knee injury.

Pro-inflammatory signaling pathways and molecules are active in all tissues within the OA joint. However, synovium and intra-articular fat are considered primary sites of inflammation. Large clinical knee imaging studies have shown that synovial and infrapatellar fat pad (IFP) inflammation are associated with a greater risk of structural disease progression [6–8], pain [9], and joint replacement surgery [10]. In patients with a meniscal injury, but without radiographic OA, synovial inflammation was present in nearly half the patients and was associated with worse pain and function [11]. Inflamed synovium had an upregulated chemokine gene expression signature associated with the recruitment of monocytes, lymphocytes, and eosinophils [11]. Indeed, $CD14^+$ monocytes and macrophages are abundant in end-stage OA synovium and IFP tissues [12–14], and activated macrophages have been detected in the joint capsule or synovium of individuals with painful knee OA [15]. Overall, macrophages appear to be critical to OA pathogenesis [16–18].

Despite these advances, macrophage-targeted therapies have not yet shown efficacy for treating OA. One factor likely limiting their success is inadequate targeting of specific cell populations. A recent single-cell RNA sequencing study involving a mouse model of post-traumatic OA identified 6 monocyte and macrophage cell populations in healthy knees, which increased to 9 populations after injury [19]. Understanding the tissue micro-environments where these cells reside, such as synovium versus IFP or perivascular versus interstitial, may aid in the development of targeted therapies. However, *tissue-specific* single-cell RNA sequencing or high-dimensional flow cytometry are not practical in murine models of OA due to tissue and cell number limitations. Recent advances in spatially resolved high-dimensional protein imaging methods provide opportunities to identify complex cell phenotypes in tissue micro-environments [20,21].

The goal of this study was to develop an imaging mass cytometry method for mice to spatially examine immune cell populations in the IFP and synovium following a non-invasive compression knee injury. Imaging mass cytometry simultaneously resolves multiple proteins in fixed, paraffin-embedded tissue sections using antibodies conjugated with unique heavy metals. Our analysis included 19 proteins to identify cell nuclei, cell proliferation, blood vessels, nerves, fat, synovial fibroblasts, and myeloid-lineage immune cells. This exploratory analysis identified diverse myeloid cell subsets that were distinct between IFP and synovium tissue and were differentially altered 2-weeks after injury. At this time-point, the acute post-injury influx of myeloid cells has largely resolved [19], potentially revealing early cellular mediators of the transition to chronic joint inflammation.

2. Methods

2.1. Experimental procedures

All experiments were conducted following a protocol approved by the AAALAC-accredited Institutional Animal Care and Use Committees at Oklahoma Medical Research Foundation (OMRF) and Oklahoma City VA. Fifteen male C57BL/6 mice were purchased from Charles River Laboratories (Wilmington, MA) at 10–11 weeks of age. Mice were group housed at OMRF (≤5 animals/cage) in specific pathogen-free conditions under a 14/10 light cycle and standard temperature conditions (21–23 °C) with *ad libitum* access to stock chow (5053, LabDiet) and chlorinated water

(0.8–1.6 ppm). At 16 weeks of age, mice were switched to a high fat diet (45 % kcal fat, Research Diets D12451i). Body weights were recorded weekly, and animal technicians performed daily health checks. At 24 weeks of age, mice were randomly assigned to sham, 0.88 mm displacement, or 1.7 mm displacement injury groups (n = 5/group). Knee injury was induced using an electromagnetic materials testing machine (Bose ElectroForce 3100, Eden Prarie, MN, USA) to apply a single compression load while mice were anesthetized with isoflurane (details in supplemental methods). A 0.6 N pre-load was held for 30 s followed by a ramp displacement of −0.88 mm or −1.7 mm at -1 mm/s using WinTest Software (TA Instruments, New Castle, DE, USA). The sham group only received the pre-load. Anterior cruciate ligament (ACL) injury was detected by auditory and mover-displacement cues in the 1.7 mm displacement group only (Fig. 1A). Two weeks following loading, animals were anesthetized using isoflurane inhalation (3–5%) for terminal blood collection by cardiac puncture. Serum was stored in aliquots at −80 °C until analysis. Following death, hindlimbs were dissected and prepared for histology and imaging mass cytometry as described in supplemental methods. To improve analysis consistency, the sample with the poorest sectioning quality or orientation was removed from each group prior to grading, resulting in n = 4 per cohort. Two graders evaluated cartilage pathology, and three graders evaluated synovial pathology (Supplemental Fig. 2); all graders were blinded to sample identification. Scores were averaged across graders to calculate a final score per sample.

2.2. Antibody selection and validation

Antibodies were selected to identify tissue-specific cells and to characterize cellular mediators of fibrosis and inflammation. We evaluated 34 different antibodies using an iterative batch testing process at various concentrations using spleen and knee joint sections prepared with multiple antigen retrieval methods. If attempts to optimize poorly detected antibodies or antibodies with high background were unsuccessful, the antibody was removed from the panel. The final panel contained 19 antibodies, which included markers for cartilage, bone, fat, vasculature, nerves, monocyte/macrophage cells, mature myeloid cells, and fibroblasts (Supplemental Table 1). Mouse spleen sections were used as positive controls for immune markers. Additional details about antibody validation are provided in Supplemental Materials.

2.3. Imaging mass cytometry

Slides were prepared for antibody staining as described in supplemental methods. Following antigen retrieval and blocking, the 19-panel metal-conjugated antibody cocktail (Supplemental Table 1) was added to the sections and incubated overnight at 4 °C. Slides were washed in PBS and stained with 125 μM Intercalator-Ir nuclear stain at room temperature for 30 min. Slides were then washed and air-dried for 20 min before loading into the Hyperion Imaging System (Standard Bio-Tools, South San Francisco, CA, USA). Regions of interest (ROI) for laser ablation were selected based on transmitted light images and stained histology images from adjacent sections. Raw mass cytometry data were acquired for each 1 μm^2 pixel within the ROI to generate MCD image files, which were visualized using MCD Viewer (Standard Bio-Tools). Data were exported from MCD viewer as a multi-OME tiff of all working channels and DNA.

2.4. Imaging mass cytometry data analysis

Multi-OME tiff files were imported into HALO software (v3.5, Indica Labs, Albuquerque, NM, USA) to identify cell nuclei with the HighPlex FL analysis module (v4.2.3) using the Iridium DNA stain. Results were exported to CellProfiler software (v3) [22] to generate cellular object masks around each nuclei identified in HALO by increasing the distance around the nuclear boundary by 5 μm. Cell Mask and Multi-OME tiff files

for each ROI were then loaded into IMACytE software [23], and a t-distributed stochastic neighbor embedding (t-SNE) dimensionality reduction analysis with arcsin transformation was completed for normalization and cluster analysis. The number of clusters were manually adjusted until the phenotypes identified in the cluster heatmaps demonstrated plausible biological separation of true phenotypes. Representative images and cell counts per cluster that were present in each test group were exported for summary statistics. Nearest neighbors and neighborhood analyses were processed in IMACytE along with summary heatmaps, glyphs, and representative images.

2.5. Statistical analysis

Given the exploratory nature of this study, a power analysis was not conducted *a priori*. However, the total sample size used for cell cluster identification by imaging mass cytometry analysis (n = 12) is consistent with prior studies in other rheumatic diseases [24,25]. Histologic grading differences between injury groups were inferred using Kruskal-Wallis test followed by Dunn's multiple comparisons test, if $p < 0.05$. Total cell count differences due to injury were inferred using one-way ANOVA, and cluster-specific cell counts were analyzed by repeated measures two-way ANOVA with Tukey's multiple comparison post-hoc test. Serum data were log-transformed for one-way ANOVA analysis. Data sets used for ANOVAs were evaluated for Gaussian distribution and homogeneous variance. Inferential uncertainty was further evaluated by 95 % CI of between-group differences. Box plots show values for individual animals, where boxes represent the 25th-75th percentiles, horizontal line the median, and whiskers indicate maximum and minimum values. Statistical analyses were performed in Prism 9.3.1 (GraphPad Software, Inc) or JMP Pro 16.0.0 (SAS Institute, Inc).

3. Results

3.1. Changes in serum inflammation and knee pathology after injury

Both 0.88 mm and 1.7 mm displacements induced substantial peak compressive forces across the knee relative to sham, although only the 1.7 mm displacement ruptured the ACL (Fig. 1A). Two weeks after injury, the body weight of the 1.7 mm cohort was 10 % less than sham animals (−4.2 g [−8.3 to −0.22g]; mean difference [95 % CI of difference]), and the body weight of the 0.88 mm cohort was 5 % less than sham (−2.2g [−6.3 to 1.9]). Knee injury also altered serum biomarkers, with reductions in Leptin and soluble CD14 (sCD14) in the 1.7 mm cohort versus sham (Supplemental Fig. 1).

Despite nearly an 8 N peak compressive load caused by the 0.88 mm displacement, we observed minimal changes in cartilage pathology and synovitis (Fig. 1B and C). In contrast, the 1.7 mm displacement caused substantial OA pathology, including large chondrophyte formation on the anterior femur, osteophytes, cartilage loss, subchondral sclerosis, meniscus hypertrophy, IFP fibrosis, synovitis, and joint capsule thickening (Fig. 1B). Using OARSI scoring, the mean difference in medial tibia cartilage pathology was substantially greater in the 1.7 mm cohort compared to sham (5.12 [3.70 to 6.55]) or the 0.88 mm cohort (4.50 [3.08 to 5.92]) (Fig. 1C). We also observed increased synovial fibrosis and moderate synovial lining hyperplasia and subintima cellularity in the IFP following 1.7 mm injury (Fig. 1C). Tibial synovium in the medial compartment was characterized by mild hyperplasia, moderate cellularity, and variable amounts of fibrosis following 1.7 mm injury (Fig. 1C). For the imaging mass cytometry analysis, we combined data from anterior and posterior synovial ROIs to facilitate comparing synovial versus IFP cell populations following injury.

3.2. Cell cluster identification in synovium and IFP tissue

We identified 21 unique cell clusters within the synovium (Fig. 2A) and 19 clusters within the IFP (Fig. 3A) using t-SNE dimensionality

reduction analysis. Cell populations were labeled based on their heatmap marker expression patterns and their tissue localization (Figs. 2B and 3B). In both synovium and IFP tissue sections, we confirmed the identification of bone marrow stromal cells, adipocytes, vascular and perivascular cells, nerves, and collagen positive cells (e.g., bone, cartilage, and tendon). Both synovium and IFP tissue sections also contained unique cell clusters with low and high expression of the extracellular matrix protein tenascin-C (TNC).

In addition, the dimensionality reduction analysis identified multiple distinct cell populations enriched for various immune cell markers. To characterize these populations, we categorized the expression of each immune marker as high, medium, low, or negligible based on a quartile analysis of the tissue-specific cell cluster heatmap expression value (Supplemental Fig. 3). We then performed a 2-way unsupervised hierarchical cluster analysis based on the quartile expression values across the selected synovium and IFP cell populations (Fig. 4). The analysis grouped several populations with medium to high expression of LY6C, CD14, CX3CR1, and VIM and low expression of F4/80. We labeled this group as monocytes/macrophages, which included 3 synovium clusters (S5, S17, and S2) and 1 IFP cluster (IFP4). We labeled a second grouping of cell populations as mature myeloid cells, which included an F4/80^{hi} group (S4 and IFP18) and an antigen presenting cell (APC) group based on high expression of MHC II (S3 and IFP2). A third grouping contained 6 synovial and 4 IFP cell populations with various expression patterns of myeloid-associated markers, which we labeled as F4/80$^+$ or F4/80$^-$ unidentified myeloid cells. Furthermore, three IFP cell clusters (IFP7, IFP8, and IFP12) were labeled as "undefined" based on insufficient marker expression information. Finally, although not included in this separate immune cell population analysis, the synovium also contained a unique cell cluster (S21) that we labeled "collagen-positive, immune high" based on the unique combination of high collagen marker expression and medium expression of LY6C, CX3CR1, MHC II, and CD31 (Fig. 2A).

Representative synovium (Fig. 2B) and IFP (Fig. 3B) multiplexed images demonstrate staining patterns for select cellular tissue markers, immune markers, and pro-fibrotic markers for each of the experimental conditions. In both synovium and IFP tissues, there is a marked increase in staining for immune and pro-fibrotic makers in the 1.7 mm displacement condition compared to either the 0.88 mm or sham conditions. Furthermore, as indicated by the DNA staining intensity and the number of cell masks identified for phenotype clustering, cellularity substantially increased with 1.7 mm injury in both tissues. We next categorized cell clusters based on shared phenotypes within synovium and IFP tissues to evaluate the effect of injury on tissue-specific changes.

3.3. Effect of injury on tissue-specific changes in cell populations

Consistent with histological findings, 1.7 mm injury had a major effect on cell populations in the synovium and IFP. This injurious condition increased total cellularity 3.4-fold in the synovium ($p < 0.0001$) and 2.2-fold in the IFP ($p = 0.0005$) compared to sham, with no differences in total cellularity between sham and 0.88 mm displacement (Fig. 5A and B). In synovial tissue, the increased cellularity was primarily due to expansion of the vascular, TNC-positive, monocyte/macrophage, and undefined myeloid cell populations (Fig. 5A, Supplemental Table 2). Notably, two of the monocyte/macrophage sub-clusters (S5 and S17) and three of the undefined myeloid sub-clusters (S11, S12, and S14) were increased in the 1.7 mm condition compared to sham or 0.88 mm displacement (Fig. 6A, Supplemental Table 3). The synovial APC myeloid population (S3) was also modestly increased 2 weeks after injury (Fig. 6A). However, we also note that several synovial immune cell populations were not different from sham 2 weeks after injury, including a monocyte/macrophage population (S2), F4/80^{hi} myeloid population (S4), and two F4/80$^+$ undefined myeloid populations (S9 and S10). When cell cluster counts were normalized to total cell counts (Fig. 5C),
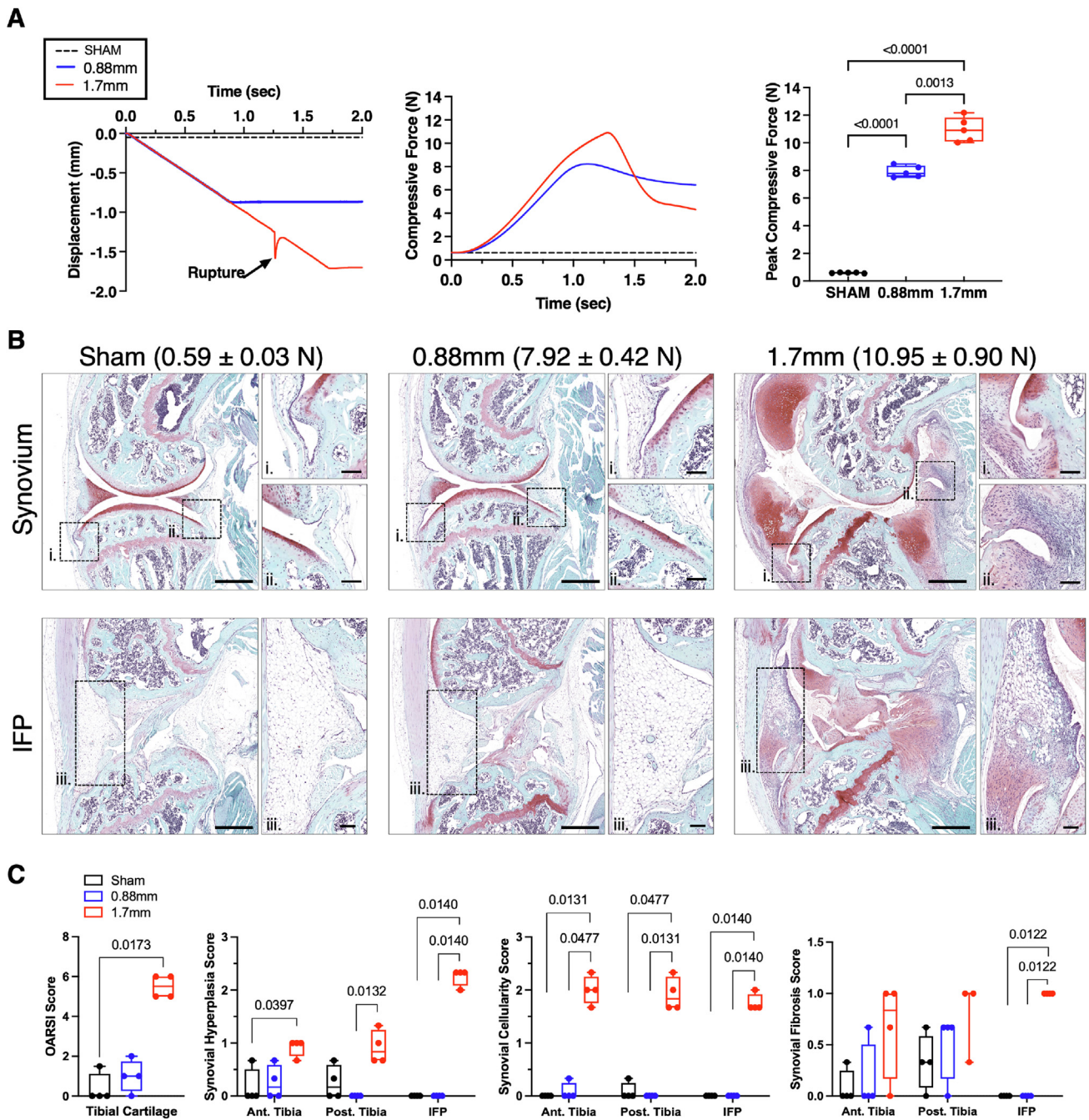
Fig. 1. Effect of non-invasive displacement injury on knee structural pathology. (A) Displacement and force characteristics from representative 0.88 mm and 1.7 mm displacement compression injury trials. Arrow in the left panel indicates the moment of ACL rupture, which was accompanied by an audible pop sound. Neither displacement nor audible cues of ACL rupture occurred during 0.88 mm displacement trials. Middle panel shows representative force versus time curves for the loading conditions. Sham loading consisted of a 30-s 0.6 N pre-load only. Right panel shows the average peak compressive loading force for all conditions. Data points represent values for individual animals. Boxes represent the 25th to 75th percentiles, horizontal line indicates the median, and whiskers demonstrate maximum and minimum values. Data analyzed by one-way analysis of variance, with Tukey's multiple comparison post-hoc test (p-values shown). (B) Representative histological images of sagittal-sectioned knee joints stained with hematoxylin, fast green, and safranin-O from each experimental group. Peak compression loads (average ± SD) are shown in parentheses adjacent to group labels. Sections were selected from the mid medial compartment for synovial analyses and mid inter-condylar region for infra-patellar fat pad (IFP) analyses. Scale bar = 500 μm. Dashed boxes identify the regions of interest (ROI's) selected for imaging mass cytometry analysis (i. = anterior tibia synovium, ii. = posterior tibia synovium, iii. = IFP). Magnified ROI images (scale bar = 100 μm) illustrate substantial cellular infiltration, synovial thickening, and IFP fibrosis due to 1.7 mm injury. (C) Semi-quantitative histological grading of cartilage and synovium pathology. Panel one shows medial compartment tibia articular cartilage OARSI scores, which were evaluated by 2 experienced graders in a blinded manner and averaged. Panels 2–4 show synovial lining hyperplasia scores (grade 0–3), synovial subintima cellularity (grade 0–3), and synovial extracellular matrix fibrosis (grade 0 or 1) for the regions of interest identified in panel A. Synovial analyses were evaluated by 3 experienced graders in a blinded manner and averaged. Data points represent values for individual animals. Boxes represent the 25th to 75th percentiles, horizontal line indicates the median, and whiskers demonstrate maximum and minimum values. Data were analyzed by Kruskal-Wallis test, with Dunn's multiple comparison post-hoc paired comparisons shown if p < 0.10. (For interpretation of the references to color in this figure legend, the reader is referred to the Web version of this article).
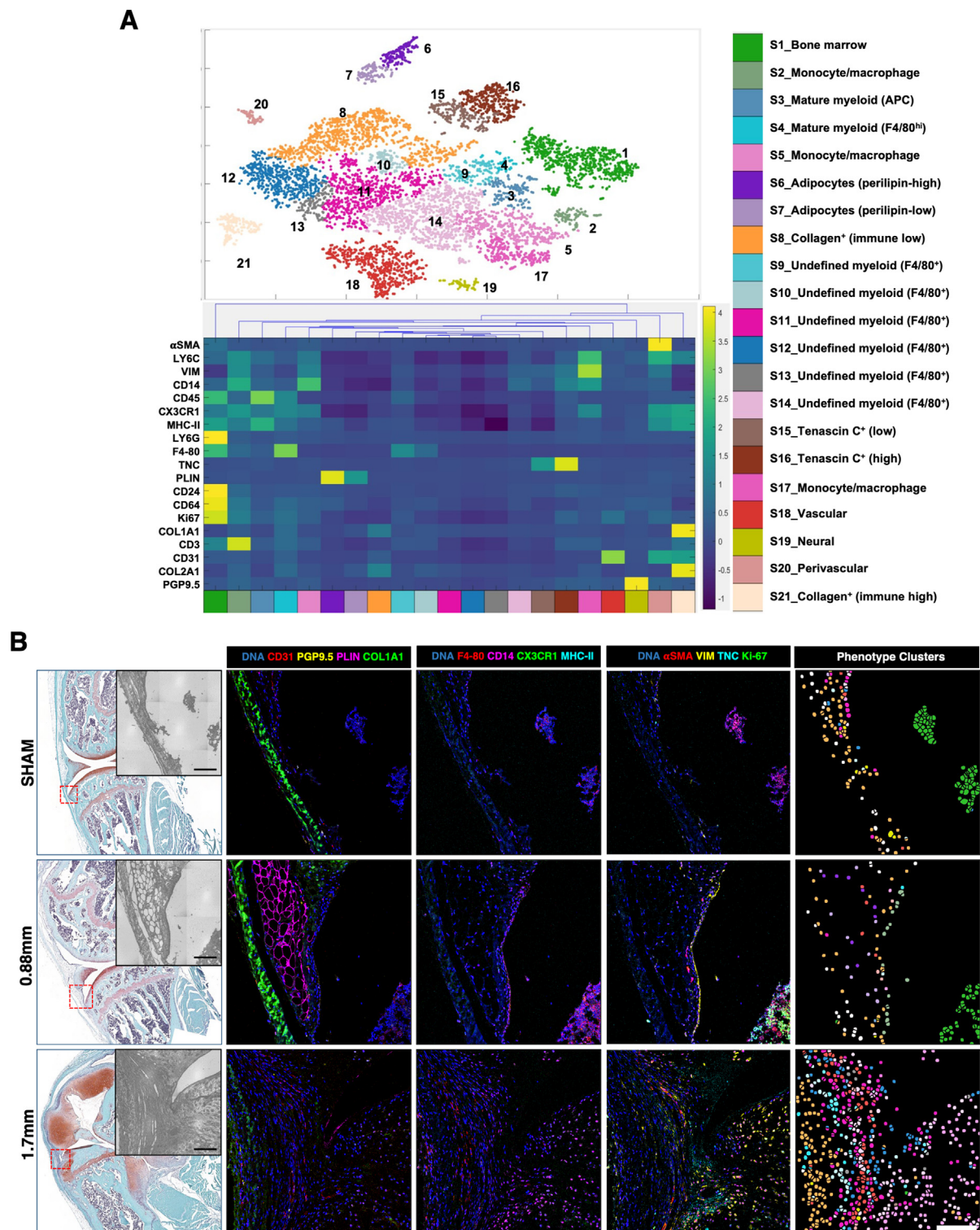
Fig. 2. Identification of synovial cell phenotypes from uninjured and injured mouse knee joints using imaging mass cytometry. (A) Unsupervised cluster analysis for identification of unique cell populations based on t-distributed stochastic neighbor embedding (t-SNE) dimensionality reduction of imaging mass cytometry marker expression data. Data points represent individual cell masks from imaging mass cytometry analyses of combined anterior and posterior tibial synovium ROIs for all experimental groups and samples. Cell cluster labels accompanying the graphical legend were based on transformed marker expression profiles shown in heatmap. Corresponding cell clusters are numerically labeled and color-matched in the t-SNE plot and graphical legend. (B) Representative examples of imaging mass cytometry cell mask identification from the anterior synovium ROI. Red square in histology image shows the approximate location of the imaging mass cytometry ROI analysis obtained from a separate serial tissue section (grey scale inset image, scale bar = 100 μm). Note that antigen retrieval processing often resulted in the loss of bone and cartilage tissue but not synovium or bone marrow. Adjacent panels show a subset of select multiplex marker expression images representing joint tissue structure (CD31, PGP9.5, PLIN, COL1A1), immune cells (F4-80, CD14, CX3CR1, MHC-II), and pro-fibrotic mediators (αSMA, VIM, TNC, and Ki-67). Final panel shows corresponding single-cell identification and phenotype cluster assignment based on legend color match in panel A. Scale bar = 100 μm. (For interpretation of the references to color in this figure legend, the reader is referred to the Web version of this article).
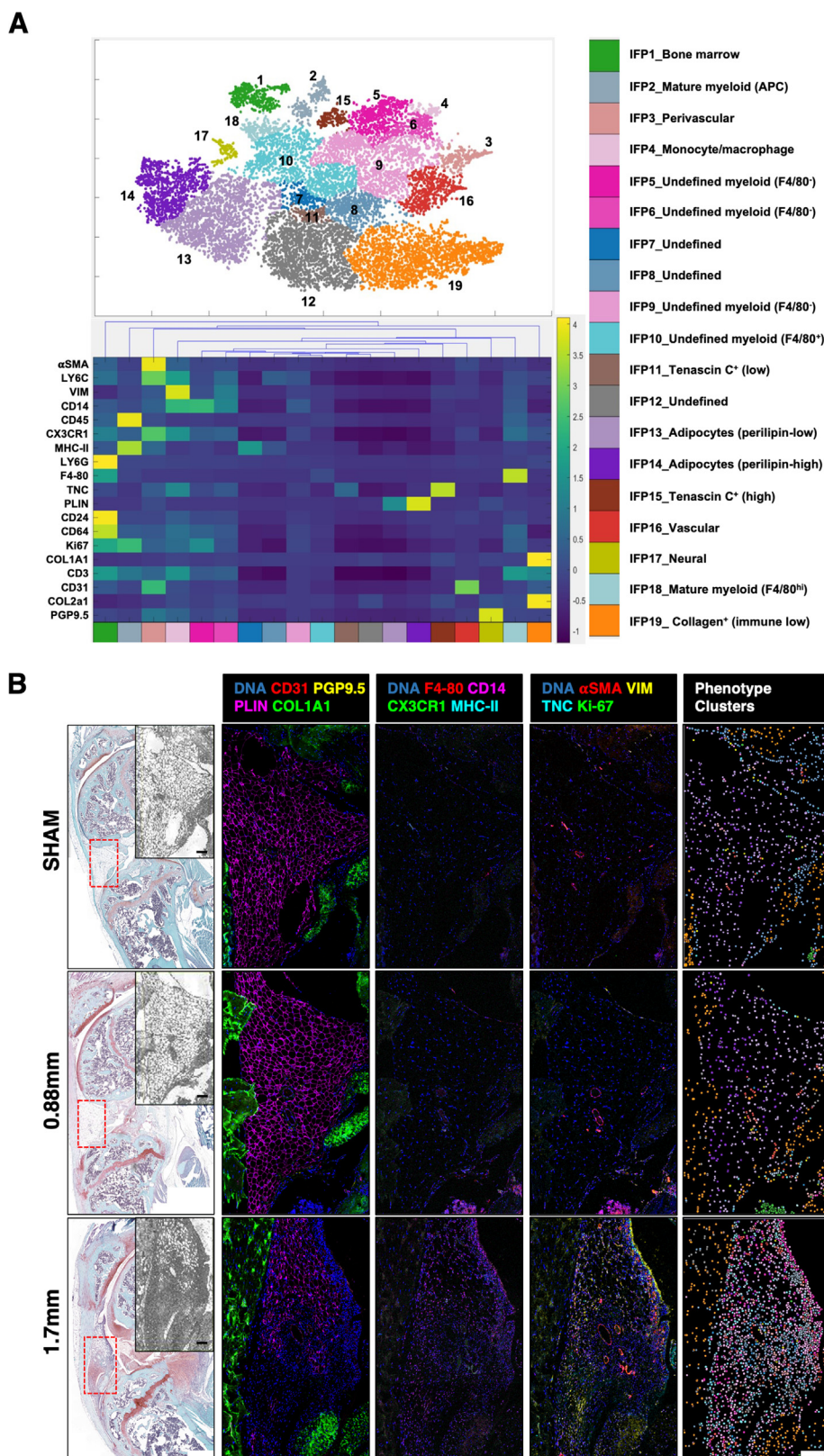
Fig. 3. Identification of infrapatellar fat pad (IFP) cell phenotypes from uninjured and injured mouse knee joints using imaging mass cytometry. (A) Unsupervised cluster analysis for identification of unique cell populations based on t-distributed stochastic neighbor embedding (t-SNE) dimensionality reduction of imaging mass cytometry marker expression data. Data points represent individual cell masks from imaging mass cytometry analyses of IFP ROIs for all experimental groups and samples. Cell cluster labels accompanying the graphical legend were based on transformed marker expression profiles shown in heatmap. Corresponding cell clusters are numerically labeled and color-matched in the t-SNE plot and graphical legend. (B) Representative examples of imaging mass cytometry cell mask identification from the IFP ROI. Red rectangle in histology image shows the approximate location of the imaging mass cytometry ROI analysis obtained from a separate serial tissue section (grey scale inset image, scale bar = 100 μm). Adjacent panels show a subset of select multiplex marker expression images representing joint tissue structure (CD31, PGP9.5, PLIN, COL1A1), immune cells (F4-80, CD14, CX3CR1, MHC-II), and pro-fibrotic mediators (αSMA, VIM, TNC, and Ki-67). Final panel shows corresponding single-cell identification and phenotype cluster assignment based on legend color match in panel A. Note the substantial increase in cellularity in the 1.7 mm group. Scale bar = 100 μm. (For interpretation of the references to color in this figure legend, the reader is referred to the Web version of this article).

several additional trends were observed, such as a reduction in adipocytes, collagen-positive immune-low, and collagen-positive immune-high cell clusters in the 1.7 mm group versus sham (Supplemental Table 4).

As in synovial tissue, vascular and undefined myeloid cell populations were increased in the IFP at 2 weeks post injury (Fig. 5B, Supplemental Table 2). However, unlike the synovium, TNC-positive, monocyte/macrophage (IFP4), and APC myeloid (IFP2) cell populations were not different from sham (Figs. 5B and 6A). Several undefined myeloid populations were increased 2 weeks after injury, including one F4/80$^+$ population (IFP10) and two F4/80$^-$ populations (IFP5 and IFP9) (Fig. 6A, Supplemental Table 3). These cells were sparsely detected in the IFP of
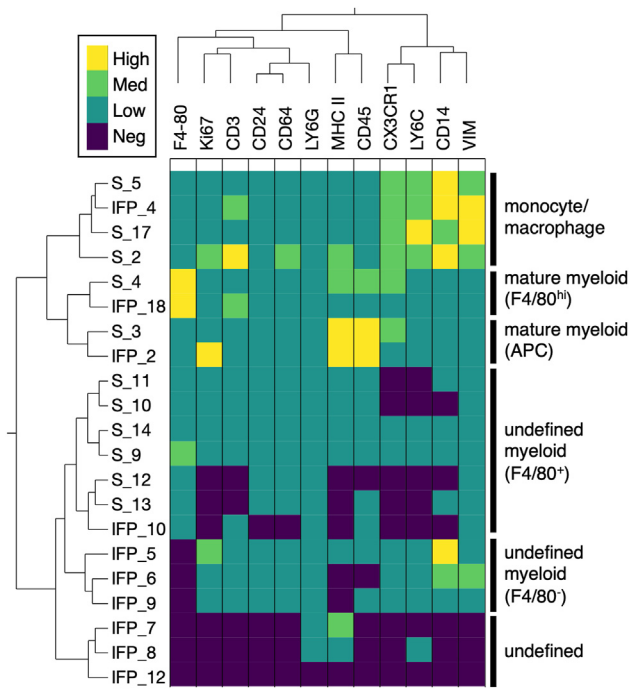
Fig. 4. Comparison and characterization of synovium and IFP cell clusters expressing markers of innate immunity. Synovium and IFP cell populations (row labels) were evaluated by two-way unsupervised hierarchical cluster analysis to facilitate identifying phenotypically similar immune cell populations in the synovium and IFP. Tissue-specific expression levels of select markers associated with innate immunity (column labels) were obtained from heatmap values show in Figs. 2A and 3A and assigned to quartile expression bins (high = 3, medium = 2, low = 1, negligible = 0) as described in Supplemental Fig. 3. Multivariate distance calculations were based on robust mean and standard deviation values from all columns combined. The resulting analysis identified synovial and IFP cell populations consistent with monocyte/macrophage cells based on medium or high expression of CX3CR1, LY6C, CD14, and VIM. Mature myeloid synovial and IFP cell populations were also identified based on high expression of F4/80 or MHC II. In addition, multiple synovial and IFP cell populations exhibited expression patterns that were distinguished as F4/80⁺ or F4/80⁻ undefined myeloid cells. F4/80 expression was not considered necessary for myeloid cell cluster classification based on recent scRNAseq analyses [19] and observed co-expression of multiple myeloid-associated markers (CD64, LY6G, CD14). Three IFP cell populations had negligible expression of most markers, which we labeled as undefined cells.

sham or 0.88 mm cohorts, but they were abundant throughout the middle of the IFP following 1.7 mm loading. We observed that IFP5 cells, which had high expression of CD14, were also enriched along the IFP-synovial lining (Fig. 6B). In addition, two undefined cell populations were expanded in the IFP 2 weeks following injury (IFP8 and IFP12). The IFP12 cell population was particularly abundant in the inferior region of the IFP (Fig. 6B), which underwent substantial changes following injury. For example, the IFP had 59 % fewer adipocyte counts in 1.7 mm versus sham conditions (p = 0.0023, Supplemental Table 2), due in large part to reduced adiposity and increased connective tissue in the inferior portion of the IFP (Figs. 1A and 3B). When cell cluster counts were normalized to total cell counts (Fig. 5C), we also observed a trend for fewer collagen-positive immune-low cells (decreasing from 27 % to 8 %) and greater TNC-positive cells (increasing from 0.1 % to 4.7 %; Supplemental Table 5).

3.4. Vascular-associated immune cell populations increase following injury

An advantage of imaging mass cytometry is the capability to explore tissue-specific changes in cellular micro-environments. We used the visual analysis tool ImaCytE to examine how frequently specific cellular

clusters spatially interacted in synovium and IFP tissues [23]. In both the synovium and IFP, collagen-positive cells (immune marker low) were spatially associated with immune cells and vascular cells in sham and 0.88 mm groups (Supplemental Figs. 4 and 5, respectively). However, with injury, myeloid cells were more likely to be spatially associated with the vasculature and other myeloid cells, and spatial associations with collagen-positive cells were less frequent.

We further explored the cell specific associations with the vasculature by testing for significant cellular micro-environment motifs centered around CD31-positive cells (Fig. 7A). These motifs, referred to as "glyphs", represent repeated patterns (>5 occurrences) of cell cluster combinations located within 10 μm of CD31-positive cells (Fig. 7B). In uninjured sham IFP tissue, there was a single CD31 glyph composed of similar proportions of other CD31-positive cells (IFP16) and αSMA-positive perivascular cells (IFP3) (Fig. 7C). However, with 1.7 mm injury, the IFP contained 3 unique CD31 glyphs composed of different combinations of monocyte/macrophages, undefined myeloid cells (F4/80⁺ and F4/80⁻), perivascular cells, and undefined cells. These glyphs were located around vasculature in the middle of the IFP and along the IFP-synovium sub-lining region. Most of these cell clusters associated with the vasculature increased in number with injury (Fig. 6B). Synovium underwent an even greater expansion in immune-associated CD31 glyphs following injury, with 9 glyphs composed of various combinations of monocyte/macrophages, mature myeloid APCs, undefined myeloid cells (F4/80⁺), and tenascin-C⁺ cells (Fig. 7D). These vascular associated cells were all more abundant than sham 2 weeks after injury (Fig. 6A).

4. Discussion

Spatially resolved high-dimensional protein imaging methods provide new opportunities to understand disease pathophysiology by identifying complex cell phenotypes in tissue micro-environments [20,21]. However, most applications in this area have been developed for human tissues. We describe the first application of an imaging mass cytometry method to examine changes in cellular composition of IFP and synovium tissues in a mouse model of post-traumatic knee OA. Two weeks after ACL rupture, cellularity was increased 2- to 3-fold in IFP and synovium tissues, primarily due to greater vascular and myeloid lineage cells. Our exploratory analysis identified multiple myeloid cell subsets that were distinct between IFP and synovium tissue, including several populations that were elevated 2 weeks after injury in a tissue-specific manner. These myeloid cell populations were associated with the vasculature in both tissues, consistent with peripheral cell infiltration. The interaction of vascular and immune cell populations was particularly diverse in the synovium, incorporating 8 unique combinations of 5 myeloid cell populations, including a monocyte/macrophage population, an MHC II^hi population, and 3 different undefined F4/80⁺ myeloid populations. Differences in synovium and IFP vascular-immune cell diversity and population sizes suggest that distinct cellular interactions drive myeloid cell infiltration, differentiation, or survival in these tissues despite other functional similarities [26–28].

Our finding of multiple myeloid cell populations in knee joint tissues is consistent with recent work by Sebastian et al. [19], who performed a comprehensive single-cell RNA sequencing analysis of immune cells isolated from whole mouse knees at multiple time points following non-invasive compression injury. The authors observed profound diversity in myeloid cells, including 9 major subtypes of monocytes and macrophages. Several subtypes were pro-inflammatory, such as MHC II^hi macrophages and multiple subpopulations of monocytes. Other subtypes exhibited anti-inflammatory and pro-repair features, such as a Lyve1^hi-Folr2^hi tissue resident macrophage subpopulation and a Trem2^hiFcrls⁺ subpopulation hypothesized to be derived from Ly6c⁺ monocytes recruited to the joint following injury [19]. Although we are do not have sufficient cellular markers to verify many subtypes, we identified a similar number of immature (e.g., monocyte and early macrophage) and
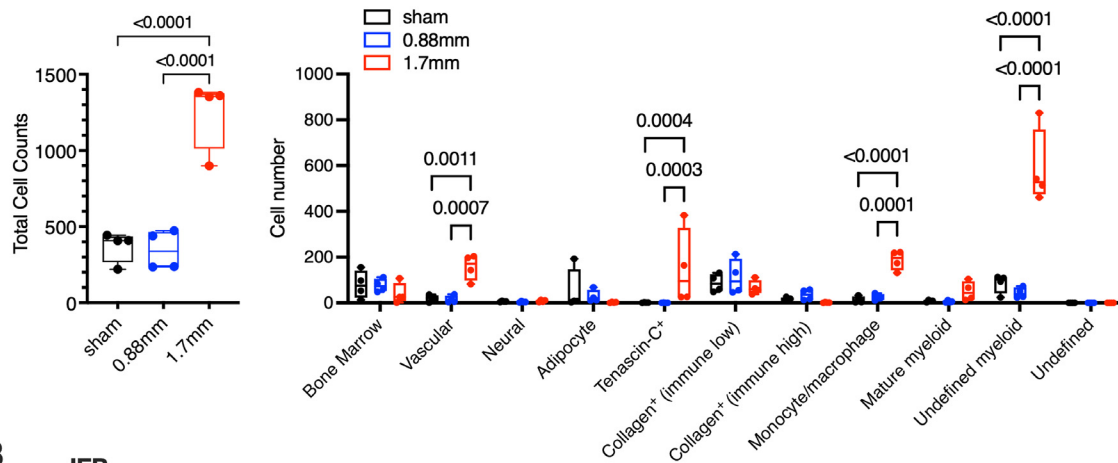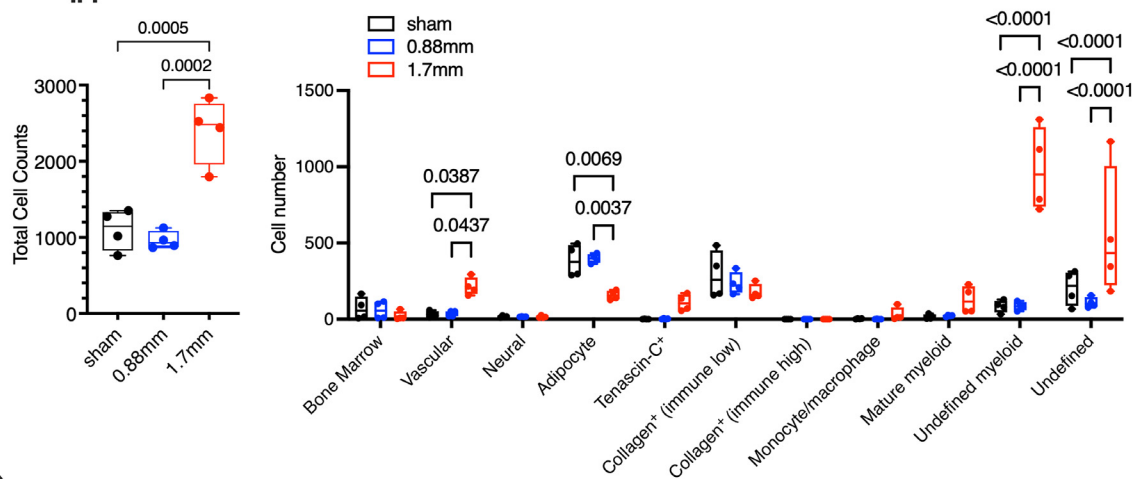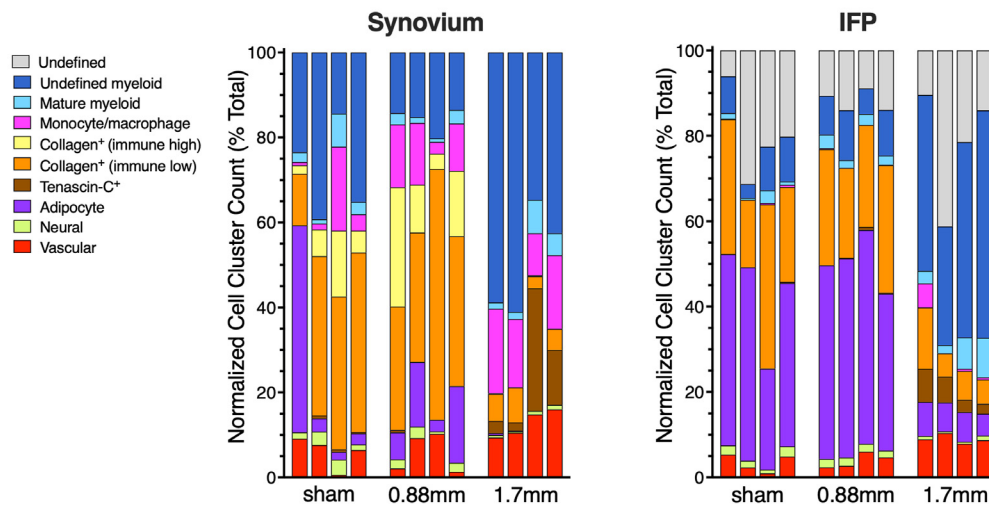
Fig. 5. Injury-dependent changes in absolute and relative cell populations in synovium and IFP tissues. (A) Total cell counts increased in the synovium following 1.7 mm displacement injury compared to 0.88 mm displacement or sham control. When cell populations were evaluated separately, the increase in cell counts with injury were due to changes in four populations: vascular cells, Tenascin-C$^+$ cells, monocyte/macrophage cells, and undefined myeloid cells. Data points represent the average anterior and posterior synovium cell population values for individual animals. Boxes represent the 25th to 75th percentiles, horizontal line indicates the median, and whiskers demonstrate maximum and minimum values. Data were analyzed by RM two-way analysis of variance, with Tukey's multiple comparison post-hoc test shown if p < 0.10. (B) Total cell counts increased in the IFP following 1.7 mm displacement injury compared to 0.88 mm displacement or sham control. When cell populations were evaluated separately, vascular, undefined myeloid, and undefined cells contributed to the increase in cell counts, offsetting adipocyte counts that decreased with injury. Data representation and statistical analyses are the same as described for panel A. (C) Stacked bar graphs of indicated cell populations expressed as a percent of the total cell counts for individual animal synovium and IFP samples (n = 4 per group). Statistical analyses of injury-dependent changes in relative cell populations are provided in main text and Supplemental Tables 4 and 5
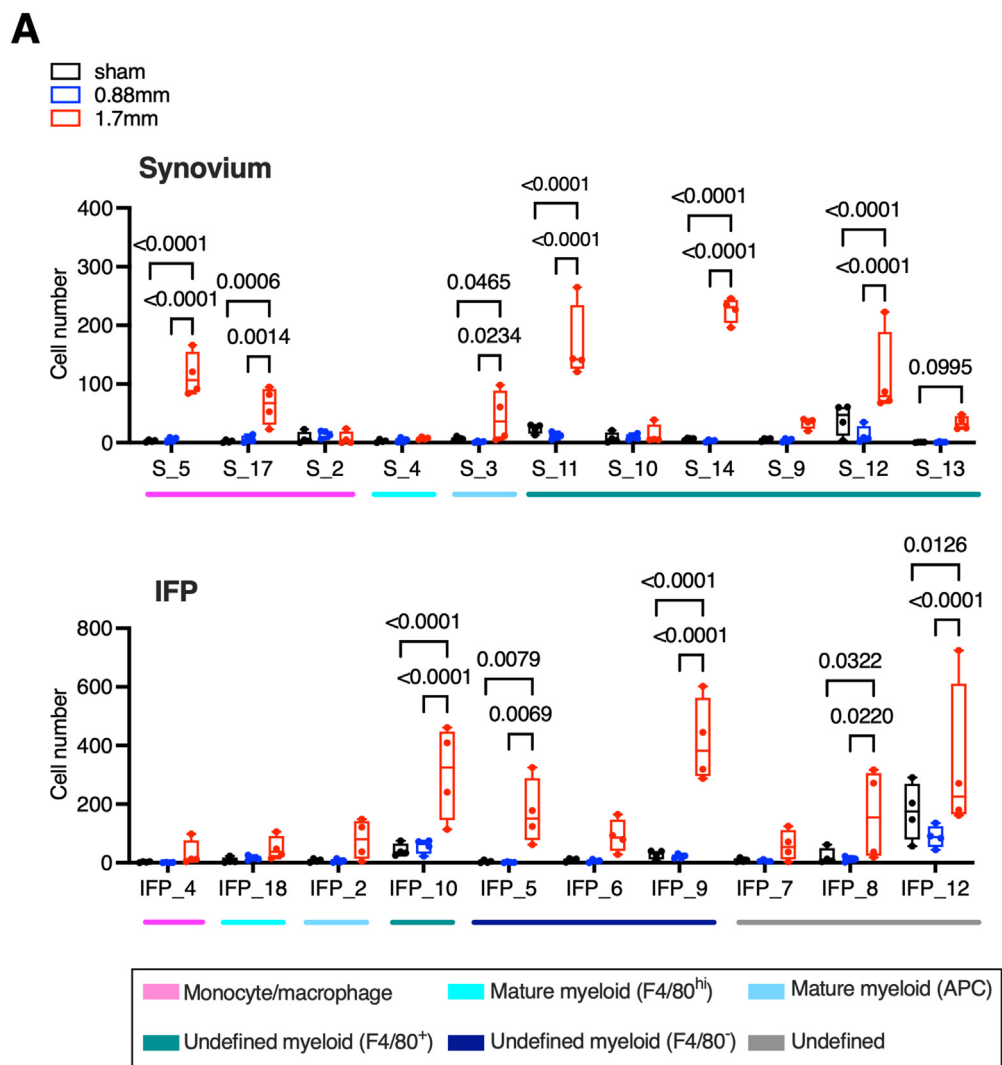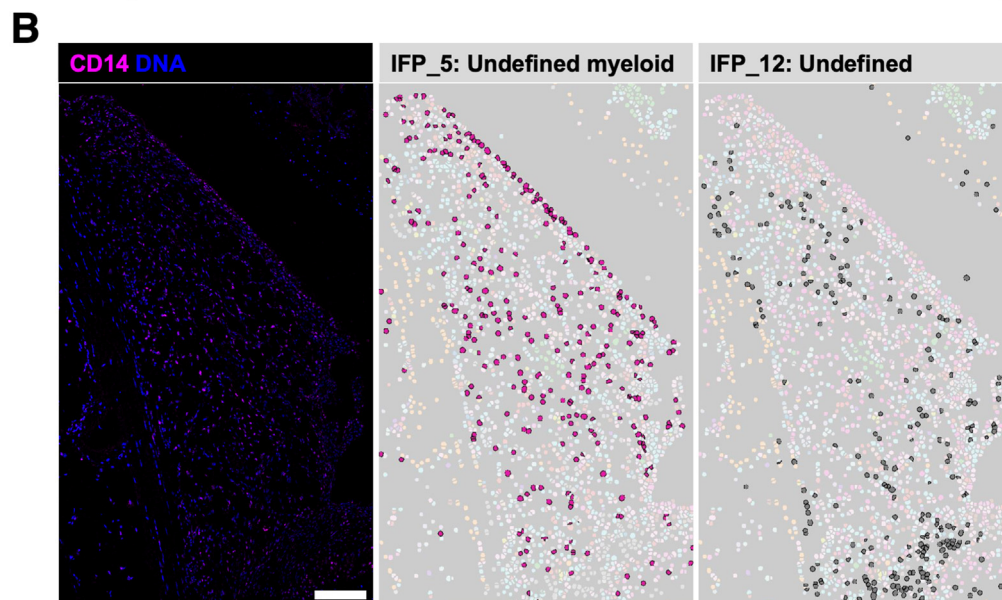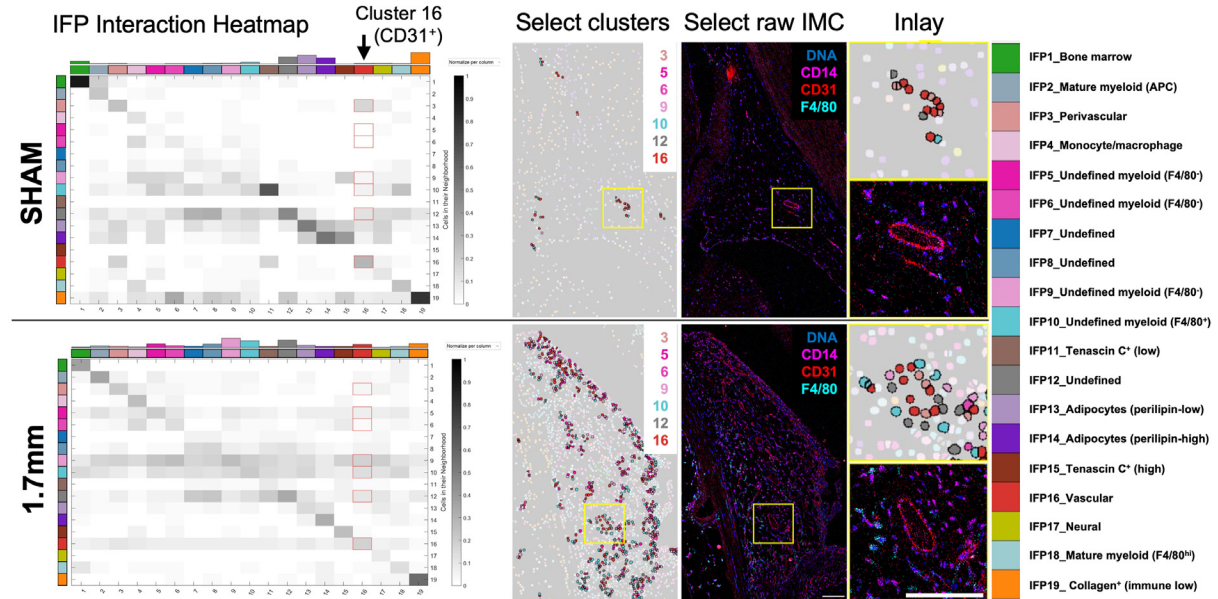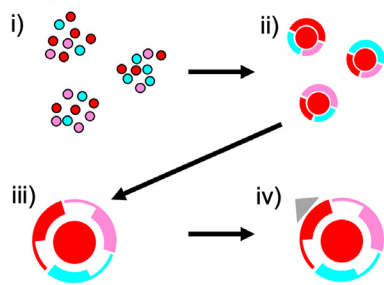
Fig. 6. Tissue-specific increases in immune cluster subsets 2 weeks post injury. (A) 1.7 mm displacement injury increased the population of distinct cell cluster subsets expressing markers of innate immunity in synovium and IFP tissues. Cell clusters are phenotypically categorized according to the color-matched horizontal bars located under x-axis labels, as defined in Fig. 4 and shown in the legend. Data points represent the average anterior and posterior synovium cell population values or the IFP cell population values for individual animals. Boxes represent the 25th to 75th percentiles, horizontal line indicates the median, and whiskers demonstrate maximum and minimum values. Data were analyzed by RM two-way analysis of variance, with Tukey's multiple comparison post-hoc test shown if $p < 0.10$. (B) Left panel shows a representative 1.7 mm IFP sample of CD14 marker expression; note expression throughout the body of the IFP and along the synovial lining. Middle panel shows the sample-matched cell masks for IFP_5, an undefined myeloid cell cluster with high CD14 expression. Note enrichment of IFP_5 cells along the synovial lining and throughout the body of the IFP. Right panel shows sample-matched cell masks for IFP_12, an undefined cell cluster increased following 1.7 mm injury. While IFP_12 cells are located throughout the injured IFP, the population is enriched in the fibrotic inferior IFP region. Statistical analyses of injury-dependent changes in relative cell populations are provided in Supplemental Tables 6 and 7 (For interpretation of the references to color in this figure legend, the reader is referred to the Web version of this article).
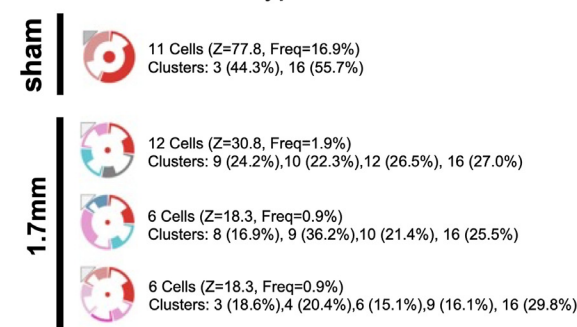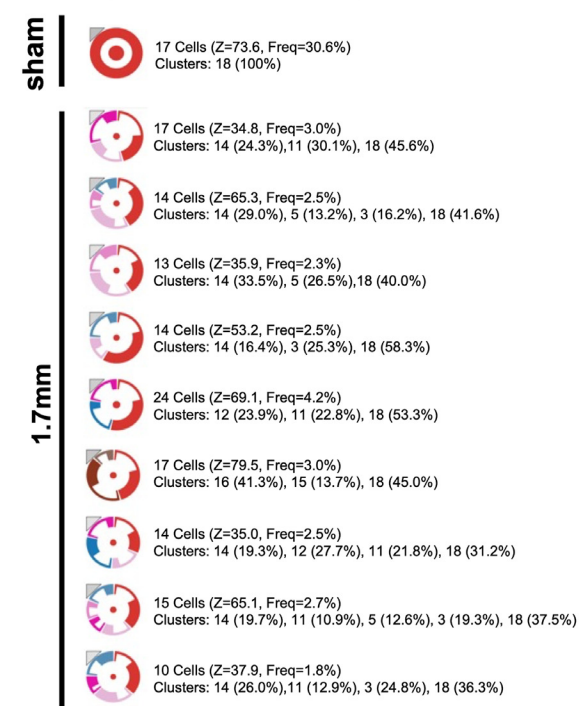
Fig. 7. Injury increases micro-environment interactions of vascular and immune cell clusters. (A) Effect of injury on select cell clusters interacting with vascular cells are highlighted in red in the heatmaps and shown as cell masks and by expression of select markers in panels to the right. Interaction heatmap graphics are normalized per column and represent the relative frequency (grayscale) that a cell cluster of interest (column) is associated with a specific cell phenotype micro-environment (row). Bar chart along top of heatmap represents the number of cells within each cluster of interest. Arrow indicates IFP_16 cluster, which is enriched for CD31 and represents vascular cells. IFP cell cluster legend is shown on the far right. (B) Example of ImaCytE glyph design representing cell cluster interactions based on Somarakis and colleagues [23]. Subpanels: (i) example of three separate vascular micro-environments, with red circles indicating the cell of interest (CD31+ vascular cells) and turquoise and pink circles representing other cell types within the vascular micro-environment; (ii) abstract representation of individual vascular glyphs, colored according to the cell of interest (center circle) and relative frequency of associated cell types (donut chart fractions); (iii) example aggregate glyph showing the mean relative frequency of associated cell types based on all micro-environments with the same cell type combinations, with variation represented by amount of cut-out of the donut chart; (iv) triangle represents statistical significance according to white-to-black color scale [23]. (C) CD31+ aggregate glyphs shown for sham and 1.7 mm conditions in the IFP, based on cell micro-environments <10 μm and >5 individual occurrences of specific cell glyphs. Associated cell clusters labeled adjacent to each glyph. (D) CD31+ aggregate glyphs shown for sham and 1.7 mm conditions in the synovium. Synovial cell cluster numbers correspond to the cluster legend provided in Fig. 2A. Injury caused a substantial, mosaic increase in vascular and immune cell micro-environment interactions. (For interpretation of the references to color in this figure legend, the reader is referred to the Web version of this article).

mature myeloid subpopulations as Sebastian et al. [19], including multiple F4/80$^+$ and F4/80$^-$ subpopulations. Notably, we observed that two synovial monocyte/macrophage subpopulations and an MHC II^{hi} population predicted to be pro-inflammatory [19] were elevated at 2-weeks post-injury, a timepoint when the inflammatory milieu transitions from an acute to chronic phase of activity in this model [19]. MHC II^{hi} myeloid cells were also present in the IFP, but they were not elevated at this timepoint. Future experiments are needed to determine if MHC II^{hi} myeloid cells are preferentially recruited to the synovium or if the regulation of MHC II expression on myeloid cells differs between these tissues.

An analysis of earlier post-injury timepoints may provide important insight into tissue-specific differences in the complex interplay between resident and infiltrating myeloid cells, including a potential role for differential chemokine and/or cytokine expression between synovium and IFP tissues. Other cell-mediated factors may also contribute to these tissue-specific differences. One potential factor is TNC, which is a large glycoprotein involved in both tissue repair and inflammation [29]. We observed an increase in TNC-positive cells in synovium but not IFP tissue at 2-weeks post-injury. The TNC antibody used in this study detects the fibronectin III alternately spliced B-domain region of TNC, a region primarily associated with fibroblast proliferation, cell migration, and extracellular matrix remodeling [30]. Further analysis of different TNC regions, isoforms, and fragments may reveal more details about mechanisms that contribute to tissue-specific pathophysiology in post-traumatic OA.

Interestingly, we observed reduced serum levels of sCD14 with injury (Supplemental Fig. 1). In patients with established knee OA, local synovial fluid sCD14 is elevated [31]. Moreover, synovial fluid sCD14 is positively associated with activated myeloid cells in the synovium, as well as with progression and severity of knee OA symptoms [32,33]. Although synovial fluid sCD14 was not measured in the present study, imaging mass cytometry revealed a robust increase in CD14^{hi} cells in the synovium (S5) and IFP (IFP5) following injury (Figs. 4 and 6). CD14 is primarily expressed by monocyte/macrophage lineage myeloid cells, and the soluble form of the molecule is derived from receptor shedding during phagocytosis and activation [34]. Thus, a concurrent reduction in serum sCD14 levels and increased local CD14^{hi} cell population may reflect recruitment of CD14$^+$ cells into the joint from the circulation. Two independent studies reported that CD14-deficient mice developed less PTOA than wild-type counterparts, suggesting that CD14$^+$ cells may be a therapeutic target for OA [35,36]. As CD14 is broadly expressed by myeloid cells, techniques that enable deeper cell phenotyping, such as imaging mass cytometry, may provide new information needed to identify the specific cell populations and tissues for therapeutic targeting.

Although the imaging mass cytometry method enabled the identification and quantification of multiple tissue-specific cellular clusters in the mouse knee following injury, there are several limitations and challenges with the method. With most imaging mass cytometry applications developed for human tissue, considerable optimization is required to develop large new panels of compatible antibodies for use in mouse, as further discussed in the Supplemental Materials. The current panel of 19 antibodies had limited phenotypic markers to functionally distinguish the numerous myeloid cell subpopulations that were identified, although efforts are ongoing to expand this panel. Given the current limitations and spatial-based cell mask analysis method used to identify cellular clusters, it is possible that some clusters labeled "myeloid" include adjacent non-myeloid immune cells or other cell types. For example, clusters S2, IFP4 and IFP 18, which show relatively high expression of CD3 in addition to moderate expression of Ly6c and CD14, could represent neighboring myeloid and lymphoid cells. The use of tissue sections rather than whole joint homogenates may also limit the detection of smaller cell populations. Finally, it is important to consider that the current biologic findings are limited to data from one post-injury time point using a single model of PTOA in male animals. Despite these limitations, our findings show that spatially resolved high-dimensional

protein imaging may be used to identify complex cell phenotypes in specific joint tissue micro-environments.

In conclusion, our imaging mass cytometry analysis indicates a high degree of complexity and tissue-specificity of synovial and IFP myeloid cells. Although additional timepoints and markers are needed to evaluate the temporal dynamics and function of these cellular populations, the current results support several important findings. First, tissue-specific myeloid populations are present in synovium versus IFP. Second, phenotypically similar myeloid populations respond differently in synovium and IFP at the same timepoint post injury. Although the IFP has a synovial lining layer, these two findings suggest that cellular interactions and signaling factors within these tissues are partly distinct. Third, myeloid populations that are elevated 2 weeks after injury, a timepoint when the inflammatory milieu transitions from an acute to chronic phase of activity in this model, are strongly associated with the vascular micro-environment in synovium and IFP. These findings provide new information about the cellular diversity and tissue specificity of individual immune cell subtypes within the joint following injury, which may aid in the development of targeted therapies for PTOA.

Contributions

All authors contributed to either the study design (SMS, MCM, PMD, CRS, TMG), acquisition of data (SMS, MCM, PMD, TS, TC, KGB, CRS, TMG), or analysis and interpretation of data (SMS, MCM, PMD, TS, TC, KGB, JMG, CRS, TMG). SMS, MCM, and TMG drafted the article, and all authors revised it critically for intellectual content. All authors approved the final version to be published.

Role of the funding sources

Conflict of interest

CRS and TMG have filed provisional patent applications #63/479,605 and #63/484,099 entitled, "COMPOSITIONS AND METHODS FOR TREATING OSTEOARTHRITIS USING A CD14 INHIBITOR".

Acknowledgements

Appendix A. Supplementary data

Supplementary data to this article can be found online at https://doi.org/10.1016/j.ocarto.2023.100416.

References

[1] T.M. Griffin, R.J. Lories, Cracking the code on the innate immune program in OA, Osteoarthritis Cartilage 28 (5) (2020) 529–531.

[2] X. Jin, J.R. Beguerie, W. Zhang, et al., Circulating C reactive protein in osteoarthritis: a systematic review and meta-analysis, Ann. Rheum. Dis. 74 (4) (2015) 703.

[3] M. Schieker, P.G. Conaghan, L. Mindeholm, et al., Effects of interleukin-1β inhibition on incident hip and knee replacement : exploratory analyses from a randomized, double-blind, placebo-controlled trial, Ann. Intern. Med. 173 (7) (2020) 509–515.

[4] F. Angelini, P. Widera, A. Mobasheri, et al., Osteoarthritis endotype discovery via clustering of biochemical marker data, Ann. Rheum. Dis. 81 (5) (2022) 666–675.

[5] A. Mahmoudian, L.S. Lohmander, A. Mobasheri, et al., Early-stage symptomatic osteoarthritis of the knee — time for action, Nat. Rev. Rheumatol. 17 (10) (2021) 621–632.

[6] S. Ramezanpour, T. Kanthawang, J. Lynch, et al., Impact of sustained synovitis on knee joint structural degeneration: 4-year MRI data from the osteoarthritis initiative, J. Magn. Reson. Imag. 57 (1) (2023) 153–164.

[7] A. Mathiessen, B. Slatkowsky-Christensen, T.K. Kvien, et al., Ultrasound-detected inflammation predicts radiographic progression in hand osteoarthritis after 5 years, Ann. Rheum. Dis. 75 (5) (2016) 825.

[8] F.W. Roemer, C.K. Kwoh, M.J. Hannon, et al., What comes first? Multitissue involvement leading to radiographic osteoarthritis: magnetic resonance imaging-based trajectory analysis over four years in the osteoarthritis initiative, Arthritis Rheumatol. 67 (8) (2015) 2085–2096.

[9] T. Neogi, A. Guermazi, F. Roemer, et al., Association of joint inflammation with pain sensitization in knee osteoarthritis: the multicenter osteoarthritis study, Arthritis Rheumatol. 68 (3) (2016) 654–661.

[10] K. Wang, C. Ding, M.J. Hannon, et al., Signal intensity alteration within infrapatellar fat pad predicts knee replacement within 5 years: data from the Osteoarthritis Initiative. Osteoarthritis and cartilage/OARS, Osteoarthritis Research Society 26 (10) (2018) 1345–1350.

[11] C.R. Scanzello, B. McKeon, B.H. Swaim, et al., Synovial inflammation in patients undergoing arthroscopic meniscectomy: molecular characterization and relationship to symptoms, Arthritis Rheum. 63 (2) (2011) 391–400.

[12] I.R. Klein-Wieringa, M. Kloppenburg, Y.M. Bastiaansen-Jenniskens, et al., The infrapatellar fat pad of patients with osteoarthritis has an inflammatory phenotype, Ann. Rheum. Dis. 70 (5) (2011) 851–857.

[13] N.S. Harasymowicz, N.D. Clement, A. Azfer, et al., Regional differences between perisynovial and infrapatellar adipose tissue depots and their response to class II and class III obesity in patients with osteoarthritis, Arthritis Rheumatol. 69 (7) (2017) 1396–1406.

[14] M.J. Wood, A. Leckenby, G. Reynolds, et al., Macrophage proliferation distinguishes 2 subgroups of knee osteoarthritis patients, JCI Insight 4 (2) (2019) 869.

[15] V.B. Kraus, G. McDaniel, J.L. Huebner, et al., Direct in vivo evidence of activated macrophages in human osteoarthritis, Osteoarthritis and cartilage/OARS, Osteoarthritis Research Society 24 (9) (2016) 1613–1621.

[16] T.M. Griffin, C.R. Scanzello, Innate inflammation and synovial macrophages in osteoarthritis pathophysiology, Clin. Exp. Rheumatol. 37 (Suppl 120) (2019) 57–63, 5.

[17] C.-L. Wu, N.S. Harasymowicz, M.A. Klimak, et al., The role of macrophages in osteoarthritis and cartilage repair, Osteoarthritis Cartilage 28 (5) (2020) 544–554.

[18] MHJ van den Bosch, PLEM van Lent, PM van der Kraan, Identifying effector molecules, cells, and cytokines of innate immunity in OA. Osteoarthritis and cartilage/OARS, Osteoarthritis Research Society 28 (5) (2020) 532–543.

[19] A. Sebastian, N.R. Hum, J.L. McCool, et al., Single-cell RNA-Seq reveals changes in immune landscape in post-traumatic osteoarthritis, Front. Immunol. 13 (2022) 938075.

[20] M.R. Eveque-Mourroux, B. Rocha, Barré Fpy, et al., Spatially resolved proteomics in osteoarthritis: state of the art and new perspectives, J. Proteonomics 215 (2020) 103637.

[21] F.J. Hartmann, S.C. Bendall, Immune monitoring using mass cytometry and related high-dimensional imaging approaches, Nat. Rev. Rheumatol. 16 (2) (2020) 87–99.

[22] A.E. Carpenter, T.R. Jones, M.R. Lamprecht, et al., CellProfiler: image analysis software for identifying and quantifying cell phenotypes, Genome Biol. 7 (10) (2006) R100. R100.

[23] A. Somarakis, V.V. Unen, F. Koning, et al., ImaCytE: visual exploration of cellular micro-environments for imaging mass cytometry data, Ieee T Vis Comput Gr 27 (1) (2021) 98–110.

[24] J. Patel, A. Ravishankar, S. Maddukuri, et al., Identification of similarities between Skin lesions in patients with antisynthetase syndrome and Skin lesions in patients with dermatomyositis by highly multiplexed imaging mass cytometry, Arthritis Rheumatol. 74 (5) (2022) 882–891.

[25] J.L. Turnier, C.M. Yee, J.A. Madison, et al., Imaging mass cytometry reveals predominant innate immune signature and endothelial–immune cell interaction in juvenile myositis compared to lupus Skin, Arthritis Rheumatol. 74 (12) (2022) 2024–2031.

[26] I.R. Klein-Wieringa, BJE de Lange-Brokaar, E. Yusuf, et al., Inflammatory cells in patients with endstage knee osteoarthritis: a comparison between the synovium and the infrapatellar fat pad, J. Rheumatol. 43 (4) (2016) 771–778.

[27] V. Macchi, E. Stocco, C. Stecco, et al., The infrapatellar fat pad and the synovial membrane: an anatomo-functional unit, J. Anat. 233 (2) (2018) 146–154.

[28] D.N. Greif, D. Kouroupis, C.J. Murdock, et al., Infrapatellar fat pad/synovium complex in early-stage knee osteoarthritis: potential new target and source of therapeutic mesenchymal stem/stromal cells, Front. Bioeng. Biotechnol. 8 (2020) 860.

[29] M. Hasegawa, T. Yoshida, A. Sudo, Tenascin-C in osteoarthritis and rheumatoid arthritis, Front. Immunol. 11 (2020) 577015.

[30] S.P. Giblin, K.S. Midwood, Tenascin-C: form versus function, Cell Adhes. Migrat. 9 (1–2) (2015) 48–82.

[31] A. Nair, V. Kanda, C. Bush-Joseph, et al., Synovial fluid from patients with early osteoarthritis modulates fibroblast-like synoviocyte responses to toll-like receptor 4 and toll-like receptor 2 ligands via soluble CD14, Arthritis Rheum. 64 (7) (2012) 2268–2277.

[32] C.A. Haraden, J.L. Huebner, M.-F. Hsueh, et al., Synovial fluid biomarkers associated with osteoarthritis severity reflect macrophage and neutrophil related inflammation, Arthritis Res. Ther. 21 (1) (2019) 146.

[33] H.N. Daghestani, C.F. Pieper, V.B. Kraus, Soluble macrophage biomarkers indicate inflammatory phenotypes in patients with knee osteoarthritis, Arthritis Rheumatol. 67 (4) (2015) 956–965.

[34] Y. Arai, K. Mizugishi, K. Nonomura, et al., Phagocytosis by human monocytes is required for the secretion of presepsin, J. Infect. Chemother. 21 (8) (2015) 564–569.

[35] Y. Won, J. Yang, S. Park, J. Chun, Lipopolysaccharide binding protein and CD14, cofactors of toll-like receptors, are essential for low-grade inflammation–induced exacerbation of cartilage damage in mouse models of posttraumatic osteoarthritis, Arthritis Rheumatol. 73 (8) (2021) 1451–1460.

[36] N. Sambamurthy, C. Zhou, V. Nguyen, et al., Deficiency of the pattern-recognition receptor CD14 protects against joint pathology and functional decline in a murine model of osteoarthritis, PLoS One 13 (11) (2018) e0206217.